Proc. 13th International Beam Instrumentation Conference,Beijing JACoW Publishing
ISBN: 978-3-95450-249-3 ISSN: 2673-5350 doi: 10.18429/JACoW-IBIC2024-WEP64

HIGH-RESOLUTION QUAD-CHANNEL PICOAMMETER: CHARACTERIZATION AND COMMISSIONING

L. Y. Tanio†, F. H. Cardoso, M.M. Donatti
Brazilian Synchrotron Light Laboratory (LNLS), Campinas, Brazil

Abstract

To address the high demand for precise low current measurements at the Sirius accelerators and its beamlines, a quad-channel high-resolution Ethernet picoammeter has been designed. The instrument can measure currents ranging from picoampere to milliampere across eight selectable ranges, featuring integrated ADCs enabling sample rates of up to 2 ksps and synchronization capabilities. This work aims to describe the design, characterization, and calibration results of the instrument. Special attention will be given to evaluating trigger latency, synchronization outcomes, as well as the device's installation and commissioning at beamlines, particularly for critical applications like on-the-fly scanning experiments. Furthermore, we will explore the interplay between trigger period, digital filter bandwidth, and front-end analog bandwidth to optimize signal-to-noise ratio in specific applications.

INTRODUCTION

This work briefly describes the hardware design, focusing on the signal path and triggered mode acquisition time analysis. There is also a discussion about the linear fit algorithm for the bandwidth and RMS current noise calculation. This paper is organized as follows: the first section discusses the hardware design, the second section presents the picoammeter operating modes, the third section performs a time analysis of triggered mode, and the fourth section presents results about the linear fitting, the trigger time analysis, and a beamline experiment. Finally, the fifth section outlines the conclusion for each section.

HARDWARE DESIGN

The quad-channel picoammeter comprises four key blocks: a current-to-voltage amplifier, an analog-to-digital converter (ADC), a microcontroller and the external interface as shown in the simplified block diagram in Figure 1. The detailed device architecture of the quad-channel picoammeter is discussed in [1].

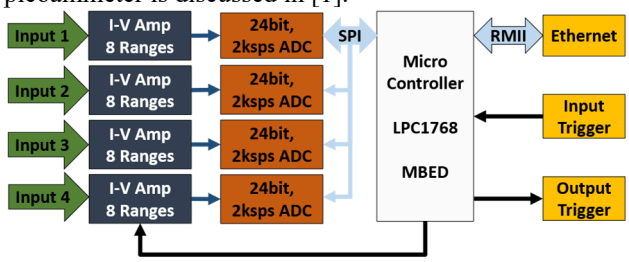

Figure 1: Quad-channel picoammeter simplified block diagram.

Analog Front-End Circuit

For each independent channel, an analog front-end circuit is composed by two fundamental blocks: the current-to-voltage amplifier, and the ADC that digitalizes the output voltage from the first block.

It is important to point out that besides the current conversion and the digitalization, both blocks also behave as low-pass filters, as shown in Figure 2.

Figure 2: Analog front-end circuit block diagram.

Current-To-Voltage Amplifier

The multi-range transimpedance amplifier was the topology selected to perform the current-to-voltage conversion due to the wide measurement range, low bandwidth applications, and noise concerns, as discussed in [1, 2].

Each current-to-voltage converter features eight selectable ranges with specific characteristics. Table 1 shows the theoretical values of the full-scale, sensitivity, and bandwidth for each selectable range.

Table 1: Transimpedance Amplifier Theoretical Characteristics: Full-Scale, Sensitivity, and Bandwidth

Scale	Full Scale	Sensitivity	Bandwidth
1	250 pA	100 pA/V	16 Hz
2	2.5 nA	1 nA/V	154 Hz
3	25 nA	10 nA/V	702 Hz
4	250 nA	100 nA/V	702 Hz
5	2.5 µA	1 µA/V	702 Hz
6	25 µA	10 µA/V	702 Hz
7	250 µA	100 µA/V	702 Hz
8	2.5 mA	1 mA/V	702 Hz

Analog-To-Digital Converter (ADC)

Considering most beamline applications: high resolution and low-speed measurements, the selected ADC features a Σ-Δ topology, 24-bit resolution, and 10 selectable sampling rates from 5 SPS to 2000 SPS. Each ADC configuration has a digital filter specification that implies different filter shapes and cutoff frequencies.

† lucas.tanio@lnls.br

ISBN: 978-3-95450-249-3 ISSN: 2673-5350 doi: 10.18429/JACoW-IBIC2024-WEP64

Microcontroller

The microcontroller, a NXP LPC1768 ARM [3] that features a 32-bit ARM Cortex-M3 core operating at up to 100 MHz with I/O capabilities, handles peripheral configuration, manages ADC data acquisition, and oversees communication for the control software infrastructure.

Input And Output Trigger

The most significant external interface in this application, apart from the communication interfaces, is the trigger interface. The picoammeter features an input optocoupler trigger that accepts a voltage range from 3.3 V to 27 V and has a minimum pulse width of hundreds of nanoseconds. It also includes an output trigger capable of driving a 50 Ω load at 5 V.

OPERATING MODES

The quad channel picoammeter has two operating modes: continuous or triggered, each with its own set of characteristics. It is important to note that each of the four channels can be individually configured to operate in either operating mode.

The continuous mode was designed to acquire samples uninterrupted at the required sampling rate. There are only two channel states: sampling or idle and two actions (or commands): to acquire or to stop.

In the triggered mode, there is another configuration, the number of samples per trigger pulse. In this mode, the ADCs sample only if the device receives a hardware or software trigger. When the number of samples sent by the ADC reaches the configured number of samples, the sampling process ceases and then the output trigger changes its logic state. In this condition, the ADC is rearmed and waiting for a new trigger.

TRIGGERED MODE: TIME ANALYSIS

The trigger time analysis starts from the input trigger's rising edge until the output trigger's rising edge. For this evaluation, four signals must be considered: the input trigger, the ADC start and data-ready pins, and the output trigger. Figure 3 shows a typical time diagram of the trigger acquisition mode when the number of samples per trigger is configured as one. The detailed explanation of the state change meaning is shown in the diagram of Figure 4.

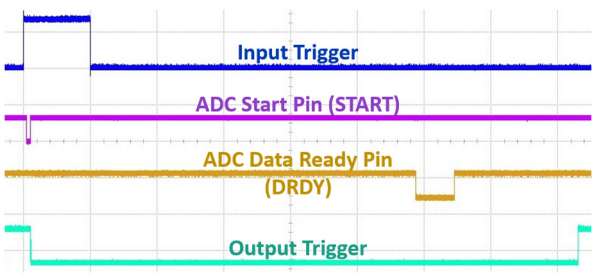

Figure 3: Time diagram in trigger acquisition mode.

The total time equation for the triggering process (Eq. (1)) can be inferred from the analysis of the time diagram (Figure 3). The description of each argument of Eq. (1) is presented in Table 2.

$$t_{tot} = t_{scd} + t_{ADC} + t_{\mu C} + t_{eth} \quad (1)$$

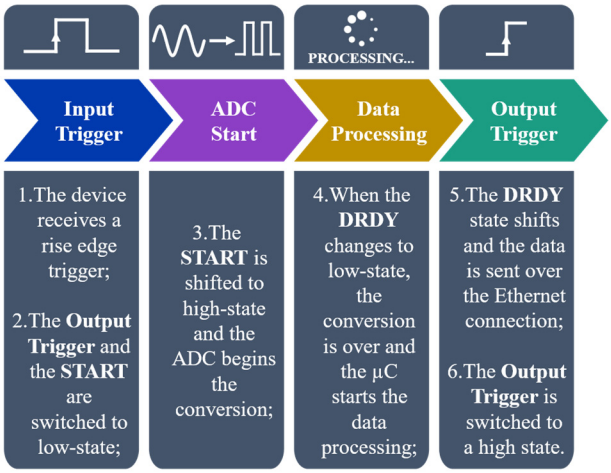

Figure 4: Step-by-step of triggering acquisition process.

Table 2: Timetable Description in Triggered Acquisition

Name	Symbol	Description
Start Conversion Delay	t_{scd}	The time interval between rising edge input trigger and rising edge START
ADC Conversion Time	t_{ADC}	The time interval between rising edge START and falling edge DRDY
Microcontroller Processing Time	$t_{\mu C}$	The time interval between DRDY falling edge and rising edge
Ethernet Circular Buffer Transfer Time	t_{eth}	The time interval between DRDY rising edge and output trigger rising edge
Total Time	t_{tot}	The time interval between rising edge input trigger and rising edge output trigger

When the acquisition process is not complete, the device firmware disregards any input trigger signals. Eq. (1) can be used to calculate the equation for the fastest trigger period, represented by Eq. (2)

$$f_{trg}^{max} = \frac{1}{t_{tot}}. \quad (2)$$

RESULTS

Bandwidth And RMS Noise

A curve fitting algorithm was developed to fully characterize each scale's bandwidth and transimpedace scale. This algorithm incorporates cutoff frequency data from the ADC datasheet [4] and the bandwidth data characterization at 2000 SPS, as described in [1]. Figure 5 shows the

ISBN: 978-3-95450-249-3 ISSN: 2673-5350 doi: 10.18429/JACoW-IBIC2024-WEP64

measured data and the curve fitting of the frequency response for each transimpedance scale at 2000 SPS.

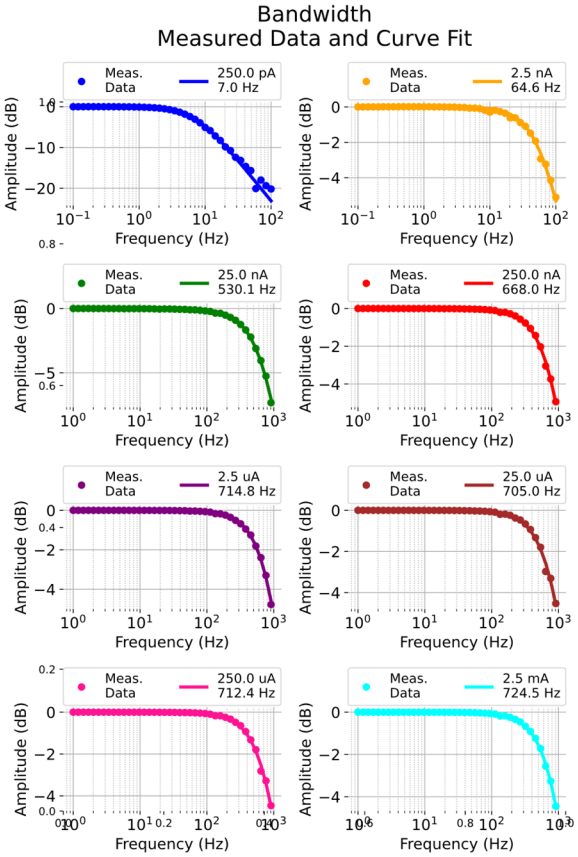

Figure 5: Frequency response at 2000 SPS. Measured data and linear fitting.

As there are more than a hundred measurements for each combination of transimpedance scale and sampling rate, the linear fitting was evaluated using the coefficient variation, which is the ratio between the mean value and the standard deviation (Eq. (3))

$$CV = \frac{\mu}{\sigma}. \tag{3}$$

As the maximum frequency coefficient variation ranges from 7 % to 10 % for any frequency combination, the variability is low.

The RMS current noise for each combination of transimpedance scale and ADC sampling frequency can be determined using Eq. (4), where bandwidth values are obtained by the curve fit and the noise spectrum density at 2000 SPS discussed in previous works [1]

$$i_n^{RMS} = \sqrt{\int_{f_{min}}^{f_c} \left(i_{n_{den}}^{RMS}\right)^2 df}. \tag{4}$$

The RMS noise dispersion was also evaluated using the variation coefficient. This metric ranges, for most bandwidth combinations, from 2 to 15 % which is a low variation. For scales 250 uA and 2.5 mA at 1000 SPS and 2000 SPS, the variation coefficient ranges from 38 to 51 %, which cannot be acceptable. For these bandwidth combinations, a further investigation must be done to track possible outliers used in the statistical analysis or to improve the curve fitting algorithm.

Figure 6 summarizes the values of the cutoff frequency (f_c) and the RMS current noise (I_n) for each sampling transimpedance scale and each ADC sampling frequency (F_s).

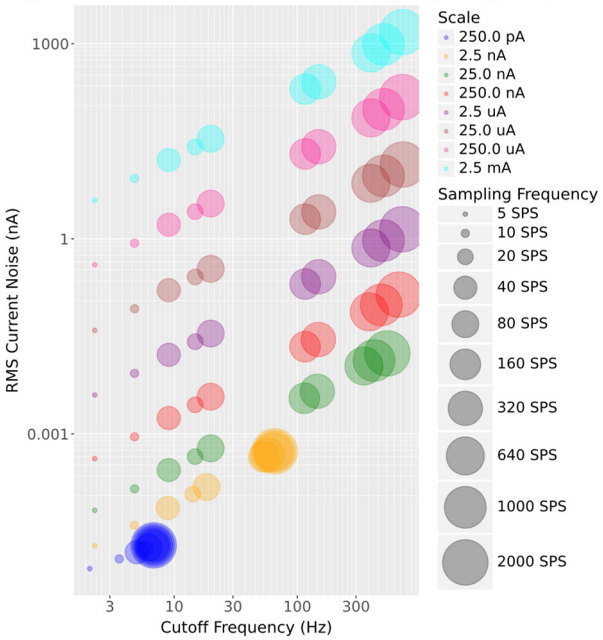

Figure 6: RMS noise current vs. cutoff frequency for each scale and sampling frequency.

Triggered Mode And Acquisition Time

The time measurements of the triggered mode acquisition were obtained using the Keysight 33220A waveform generator [5] to produce the trigger signals and the Keysight DSOS104A digital oscilloscope [6] to gather the time interval between the edges. Table 3 shows the measured time interval at 2000 SPS, four channels enabled, and one sample per trigger pulse.

Table 3: Measured Time Interval at Triggered Mode, 2000 SPS, Four Channels Enabled, and One Sample Per Trigger

Name	Time (µs)
Start Conversion Delay (t_{scd})	10.8 ± 0.3
ADC Conversion Time (t_{ADC})	577.4 ± 0.1
µC Processing Time ($t_{\mu C}$)	58.2 ± 2.6
Ethernet Time (t_{eth})	234.7 ± 17.8
Total Time (t_{tot})	881.1 ± 18.0

As t_{scd}, $t_{\mu C,}$ and t_{eth} (Table 3) are independent of the sampling rate and the t_{ADC} can be found in a lookup table in [4], it is possible to estimate a total conversion time and consequently the maximum trigger frequency for each ADC sampling rate.

Table 4 summarizes the values of the conversion time (T_{conv}), the maximum trigger frequency (F_{TrgMax}), and

ISBN: 978-3-95450-249-3 ISSN: 2673-5350 doi: 10.18429/JACoW-IBIC2024-WEP64

signal bandwidth (BW_{sig}). Eq.(2) has been used to estimate the maximum trigger frequency, taking into account two considerations: the standard deviation of t_{ADC} was neglected and the employed time was the total time mean value added to the standard deviation multiplied by 3. The signal bandwidth was calculated using Eq. (5)

$$BW_{sig} = \frac{F_{TrgMax}}{2}. \quad (5)$$

Table 4: Estimated Conversion Time (T_{conv}), Maximum Trigger Frequency (F_{TrgMax}), and Maximum Signal Bandwidth (BW_{sig}) for Each ADC Sampling Frequency (F_{TrgMax})

F_s (SPS)	T_{conv} (ms)	f_{TrgMax} (Hz)	BW_{sig} (Hz)
5	200.6	4.9	2.5
10	100.9	9.9	5.0
20	51.1	19.5	9.8
40	25.5	39.1	19.6
80	13.0	76.5	38.3
160	6.8	146.1	73.1
320	3.6	277.4	138.7
640	2.0	487.9	244.0
1000	1.4	668.6	334.3
2000	0.9	1070.0	535.0

When the cutoff frequency (f_c) from Figure 6 is compared to the signal bandwidth (BW_{sig}) from Table 4, the f_c values for the scales 25 nA, 250 nA, 2.5 µA, 25 µA, 250 µA, and 2.5 mA for sampling rates 20 SPS, 40 SPS, 80 SPS, 160 SPS, 320 SPS, 640 SPS, 1000 SPS, and 2000 SPS are greater than the BW_{sig} values. This indicates that the analog front-end bandwidth is over-designed and can be optimized to minimize the RMS current noise.

Measurements At SABIA Beamline

At the SABIA (Soft x-ray ABsorption spectroscopy and ImAging) beamline [7], the quad-channel picoammeter is essential for conducting absorption measurements. The first channel is connected to a gold mesh to measure the beam intensity (I0), and the second channel is directly connected to the sample (I1). The ratio between the I1 and I0 is the sample absorption amount.

To generate X-ray absorption spectrums, the experiments use the on-the-fly scanning technique that moves the optical elements (undulator, monochromator, and mirrors) to provide energy scanning and perform current measurements synchronously. The system response to manage the synchronization is the LNLS Timing and Trigger Unit (TATU) [8].

For each energy scanning, the number of samples and the input trigger pulses can vary from hundreds to tens of thousands of samples. Since these scans are performed a dozen times daily, and no problems have been reported with the picoammeter, this metric validates the reliability and repeatability of the instrument.

Figure 7 shows a practical problem found in a beamline experiment where the electron mobility of a specific material is low, and the measured current is noisy. An alternative to mitigate this problem is to change the ADC sampling rate to find a better signal-to-ratio response.

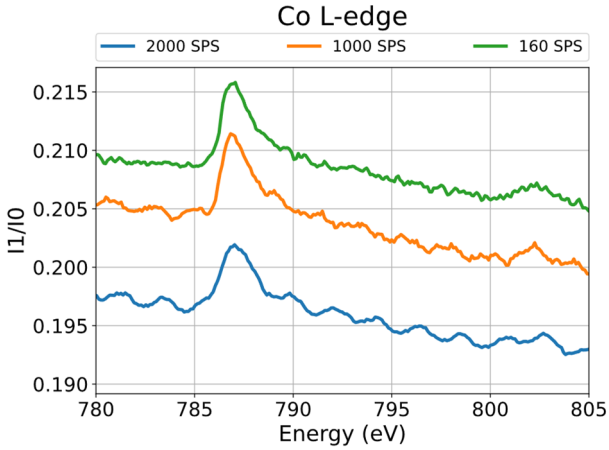

Figure 7: Cobalt (Co) L-edge Absorption Spectrum for different ADC sampling frequencies (160, 1000, and 2000 SPS) and the same acquisition time.

CONCLUSION

The picoammeter commissioning at the beamlines brought the necessity of a deeper investigation of the bandwidth characterization and the device limitations concerning the triggered mode.

The linear fit algorithm that describes the frequency response for each combination of the transimpedance scale and the ADC sampling frequency was homologated by the statistical analysis, as the variation coefficient is low. On the other hand, the algorithm that calculates the RMS current noise does not make a good fit for the scales 250 uA and 2.5 mA at 1000 SPS and 2000 SPS, as the variation coefficient are considerably high and further investigations must be performed to track possible outliers to improve the curve fitting algorithm. Nevertheless, the RMS current noise data can be used as a guide to estimate the total amount of intrinsic noise.

From the time analysis at triggered mode, it was possible to estimate the amount of time to acquire one sample, and consequently assess the maximum trigger frequency and the signal bandwidth. The comparison of this data and the combined cut-off frequency shows that the analog front-end is not optimized.

Finally, the measurements at the SABIA beamline, using the on-the-fly scan technique, validate the reliability and repeatability of the quad-channel picoammeter.

ACKNOWLEDGMENTS

The authors are grateful for the funding from the Brazilian Ministry of Science, Technology, and Innovation and the contributions of the LNLS teams, particularly the Software Control group and Sabia beamline group.

ISBN: 978-3-95450-249-3 ISSN: 2673-5350 doi: 10.18429/JACoW-IBIC2024-WEP64

REFERENCES

[1] M. M. Donatti, F. H. Cardoso, and L. Y. Tanio, "Development of a quad-channel high-resolution digital picoammeter for beam diagnostics", *IEEE Open J. Instrum. Meas.*, vol. 19, no. 03, p. C03028, Mar. 2024. doi:10.1088/1748-0221/19/03/c03028

[2] L. Y. Tanio, F. H. Cardoso, and M. M. Donatti, "A Multi-range Low Noise Transimpedance Amplifier for Sirius Beamlines", in *Proc. IPAC'21*, Campinas, Brazil, May 2021, pp. 3447-3450. doi:10.18429/JACoW-IPAC2021-WEPAB330

[3] NXP, Arm LPC1768 Board, https://www.nxp.com/products/processors-and-microcontrollers/arm-microcontrollers/general-purpose-mcus/lpc1700-cortex-m3/arm-mbed-lpc1768-board:OM11043

[4] Texas Instruments, "ADS1246: 24-Bit Analog-to-Digital Converter (ADC) for Low-Noise Sensor Measurement", ADS1246 datasheet, Sep. 2011 [Revised Jan. 2022].

[5] Keysight 33220A 20 MHz Function/Arbitrary Waveform Generator, https://www.keysight.com/us/en/assets/7018-01144/data-sheets/5988-8544.pdf

[6] Keysight DSOS104A Infiniium S-Series The Standard for Superior Measurements, https://www.keysight.com/us/en/assets/7018-04261/data-sheets/5991-3904.pdf

[7] V.B. Zilli *et al.*, "Exactly Constrained, High Heat Load Design for SABIA's First Mirror", in *Proc. 12th Int. Conf. Mech. Eng. Design Synchrotron Radiat. Equip. Instrum. (MEDSI'23)*, Beijing, China, Nov. 2023, pp. 44-47. doi:10.18429/JACoW-MEDSI2023-TUPYP008

[8] J. R. Piton *et al.*, "TATU: A Flexible FPGA-Based Trigger and Timer Unit Created on CompactRIO for the First Sirius Beamlines", in *Proc. ICALEPCS'21*, Shanghai, China, Oct. 2021, pp. 908-911. doi:10.18429/JACoW-ICALEPCS2021-THPV021